


Dynamics and phase separation of active Brownian particles on curved surfaces and in porous media

Priyanka Iyer^{ⓧ,*}, Roland G. Winkler^{ⓧ,†}, Dmitry A. Fedosov^{ⓧ,‡}, and Gerhard Gompper^{ⓧ,§}
*Theoretical Physics of Living Matter, Institute of Biological Information Processing and Institute for Advanced Simulation,
 Forschungszentrum Jülich, 52425 Jülich, Germany*

 (Received 15 December 2022; accepted 7 June 2023; published 26 July 2023)

The effect of curvature on an ensemble of repulsive active Brownian particles (ABPs) moving on a spherical surface is studied. Surface curvature strongly affects the dynamics of ABPs, as it introduces a new time scale $\tau = R/v_0$, with curvature radius R and propulsion velocity v_0 , in addition to the rotational diffusion time τ_r . The time scale τ is related to a stop-and-go motion caused by the recurrent alignment of the propulsion direction with the surface normal. This implies that motility-induced phase separation (MIPS) disappears for small R . Furthermore, it causes a narrowing of the MIPS regime in the phase diagram of Péclet number Pe and particle area fraction ϕ . Also, the phase-separation boundary at low ϕ attains a turning point at small R , allowing for the possibility of a reentrant behavior. For a system of two pores with unequal radii connected by a small passage, the density in each pore is found to be inversely proportional to local particle mobility. Notably, this relation breaks down when MIPS occurs in either sphere or when the noise is high. ABPs move against the density gradient owing to their spatially varying velocity. The magnitude of the directional flux from one pore to the other is proportional to the particles effective diffusion constant in the pore. Moreover, fluctuations in the number of ABPs within the pores near the MIPS transition are found to induce transient MIPS states.

DOI: [10.1103/PhysRevResearch.5.033054](https://doi.org/10.1103/PhysRevResearch.5.033054)

I. INTRODUCTION

Ensembles of self-propelling particles display rich dynamical behaviors, which arise from their out-of-equilibrium nature [1–3]. A prominent example is motility-induced phase separation (MIPS) in systems with no attractive or alignment interactions between the particles, which have been studied in detail for active Brownian particles (ABPs) both in simulations [4–9] and experiments [10–12]. In more complex systems, several other factors have been found to affect and modify the onset of activity-induced clustering, such as shape anisotropy [13–19], hydrodynamic interactions [20–23], deformability of the confinement [24,25], and dimensionality [26,27].

In biophysical systems, active particles are often exposed to curved geometries and confinement. Examples include bacteria motion in porous media [28], cell migration on curved tissues of the gut [29], embryonic development [30], and actomyosin flows during cell division [31]. Theoretical studies of single active particles indicate that for a tangential

propulsion direction, their dynamics depends on the surface curvature [32,33], while for an unconstrained propulsion direction, particles predominantly accumulate in regions of higher curvature [34,35]. Steric interactions among active elongated particles, which favor polar or nematic alignment, generate complex flow patterns on spherical geometries, such as circulating band states [36–38]. Further studies have shown topology-dependent collective dynamics of self-propelled rods [39], as well as segregation dynamics in binary mixtures of active and passive particles on spherical surfaces [40].

We study here the dynamics and clustering behavior of repulsive ABPs, with a freely diffusing propulsion direction, but constrained to move on a curved surface in two/three spatial dimensions (2D/3D). We show that the confinement radius R introduces a new time scale that changes qualitatively the dynamics of ABPs on curved surfaces, such that their ballistic motion for large Péclet numbers Pe is suppressed at distances smaller than R , where $Pe = v_0\tau_r/\sigma$, with propulsion velocity v_0 , rotational diffusion time $\tau_r = D_r^{-1}$ and rotational diffusion coefficient D_r , and ABP diameter σ . The diagram of phase separation on a sphere is constructed, and shows that curvature drastically changes the phase boundaries, and completely suppresses MIPS at small R . A simple model that considers the effective persistence length of particle motion on the sphere is then used to rationalize the observed effects of sphere curvature on MIPS.

Furthermore, we study MIPS in porous media, represented by a paradigmatic example of two spheres with unequal radii connected by a small passage. We find that for large Pe and small particle numbers, the density within each pore is inversely proportional to its tangential velocity, similar to other

*p.iyer@fz-juelich.de

†r.winkler@fz-juelich.de

‡d.fedosov@fz-juelich.de

§g.gompper@fz-juelich.de

studies of active matter systems [41,42]. However, MIPS in the pores destroys this correlation due to reduced particle densities near the passage. As ABP number is increased, MIPS occurs first in the smaller pore, followed by the larger pore. There can be intermittent MIPS for moderate Péclet numbers driven by the particle fluxes between the two spheres. A steady-state exchange flux of ABPs through the passage is found to decrease with increasing Pe, due to the reduced effective diffusion constant of ABPs. Importantly, we find that Péclet number and not velocity determines the dimensionless flux between the two pores. The flux initially increases with increasing particle number. However, MIPS leads to lowered density near the passage and consequently to a sudden decrease in the particle fluxes.

II. MODEL AND METHODS

Self-propelled particles are simulated as active Brownian particles (ABPs) embedded in 3D but restricted to move on a two-dimensional spherical surface. An ABP experiences a propulsion force f_p acting along its orientation vector \mathbf{e}_i . The equation of motion for the position \mathbf{r}_i of an ABP is given by

$$m\ddot{\mathbf{r}}_i = f_p \mathbf{e}_i - \gamma \dot{\mathbf{r}}_i - \nabla_i (U_{\text{conf}} + U_{\text{int}}), \quad (1)$$

where m is the particle mass, γ is the friction coefficient, U_{conf} is the confinement potential, U_{int} is the pairwise interaction potential between different ABPs, and ∇_i is the spatial derivative at particle i . The orientation vector \mathbf{e}_i is subject to a diffusive rotation modeled as

$$\dot{\mathbf{e}}_i = \boldsymbol{\zeta}_i \times \mathbf{e}_i, \quad (2)$$

where $\boldsymbol{\zeta}_i$ is a Gaussian and Markovian random process with $\langle \boldsymbol{\zeta}_i(t) \rangle = 0$ and $\langle \boldsymbol{\zeta}_i(t) \cdot \boldsymbol{\zeta}_i(t') \rangle = 6D_r \delta_{ij} \delta(t - t')$ with a rotational diffusion coefficient D_r . Note that we neglect the effect of translational noise in Eq. (1). The confinement and particle-particle interactions are represented by the Lennard-Jones (LJ) potential as

$$U(r) = \begin{cases} 4\epsilon \left[\left(\frac{\sigma_{LJ}}{r} \right)^{12} - \left(\frac{\sigma_{LJ}}{r} \right)^6 \right], & \text{if } r < r_c, \\ 0, & \text{if } r \geq r_c, \end{cases} \quad (3)$$

where σ_{LJ} is the distance at which $U(\sigma_{LJ}) = 0$ and ϵ is the potential strength. For the confinement interactions, the cut-off radius is set to $r_c = 2^{1/6} \sigma_{LJ}/2$, while for the ABP-ABP interactions, $r_c = 2^{1/6} \sigma_{LJ}$, so that interactions between particles are purely repulsive. Confinement of the ABPs to a two-dimensional spherical surface of radius R is achieved by placing two concentric spherical surfaces with radii $R \pm \sigma_{LJ}/2$ at which the LJ potential is centered. Similarly, confinement of ABPs to a ring geometry (particle is embedded in 2D and restricted to move in 1D) is achieved with two repulsive concentric rings.

Activity of the ABPs is described by the dimensionless Péclet number $\text{Pe} = f_p / (\gamma \sigma D_r) = v_0 \tau_r / \sigma$, where $\sigma = 2^{1/6} \sigma_{LJ}$ is the ABP diameter and $f_p = \gamma v_0$, where v_0 is the ABP velocity. The propulsion force (velocity) is kept constant, with $v_0 = 0.5$ ($\gamma = 1$) and Pe is varied through the rotational diffusion time τ_r . This implies that the effective ABP diameter does not decrease with increasing Pe [44] (for details see Appendix B). Moreover, we have $\tau_{\text{relax}} \ll \tau_r$ and $\tau_{\text{relax}} \ll$

σ/v_0 , where $\tau_{\text{relax}} = m/\gamma$ is the relaxation time, so that we are in the overdamped regime. The surface density of the ABPs on a sphere is given by $\phi = N\sigma^2/(16R^2)$, where N is the total number of ABPs.

III. RESULTS

A. Single ABP dynamics

We consider first a model of an ABP as a disk of diameter σ in 2D, confined to a ring of radius R . While the ABP motion is restricted to 1D, the propulsion vector \mathbf{e} is free to rotate in 2D, see Fig. 1(a). Then, the equations of motion (1) and (2) for the position $\mathbf{r} = (R \cos \theta, R \sin \theta)$ and propulsion direction $\mathbf{e} = (\cos \psi, \sin \psi)$ of the ABP become

$$\dot{\theta} = -\frac{v_0}{R} \sin(\theta - \psi), \quad \dot{\psi} = \sqrt{2D_r} \Gamma_\psi, \quad (4)$$

where θ is the positional angle, ψ is the orientational angle, and Γ_ψ is the rotational noise with $\langle \Gamma_\psi \rangle = 0$ and $\langle \Gamma_\psi(t) \Gamma_\psi(t') \rangle = \delta(t - t')$.

In the limit of small misalignment angles $\delta \equiv \theta - \psi$, with $|\delta| \ll 1$, Eq. (4) can be linearized and analytically solved (Appendix A), resulting in the angular mean-squared displacement (MSD)

$$\langle (\theta(t) - \theta(0))^2 \rangle = 2D_r t - \frac{2D_r R}{v_0} (1 - e^{-v_0 t/R}). \quad (5)$$

Thus, irrespective of τ_r , the crossover between the diffusive and ballistic regime is determined by the new time scale $\tau = R/v_0$, see Fig. 1(b). The shift of the onset of the diffusive behavior to earlier times for smaller radii R originates from a fast alignment of particle orientation with the surface normal, as the ABP moves along the surface, upon which the translational motion of the particle nearly stops [45].

The discussion above suggests that the misalignment angle δ plays an essential role. The Fokker-Planck equation (Appendix A) corresponding to the Langevin equations (1) and (2) yields the stationary-state distribution

$$P(\delta) = \frac{1}{2\pi I_0(\tau_r/\tau)} \exp\left[\frac{\cos \delta}{\tau D_r}\right]. \quad (6)$$

In the limit $\tau/\tau_r \ll 1$, we obtain $\langle \delta^2 \rangle = \tau/\tau_r = R/(\sigma \text{Pe})$. For the tangential velocity $v_t = v_0 |\sin(\delta)|$, this implies that $\langle v_t \rangle \simeq v_0 \sqrt{\tau/\tau_r}$. Thus, the ABP slows down with increasing curvature (or decreasing τ), which is also reflected in Eq. (5) where the MSD in the ballistic regime is given by $R^2 \langle [\theta(t) - \theta(0)]^2 \rangle = \langle v_t \rangle^2 t^2$. Figure 1(c) shows excellent agreement of the distribution of the misalignment angle from the linearized theory and the corresponding simulations.

In 3D, the dynamic behavior of ABPs and the corresponding MSD are more complex, as both time scales τ and τ_r become important due to an additional angular degree of freedom. The (positional) MSD in Fig. 2 shows that the ratio $\tau_r/\tau = \sigma \text{Pe}/R$ determines the particle dynamics. For $\tau_r/\tau \ll 1$, the ABP does not notice the effect of curvature and exhibits ballistic motion for times less than τ_r . However, when $\tau_r/\tau \gg 1$, the particle moves ballistically only up to the shorter time τ . For $t > \tau$, diffusive motion due to sphere curvature dominates, and can be described as a stop-and-go motion due to fast alignment of \mathbf{e} along \mathbf{r} . Figure 2 also

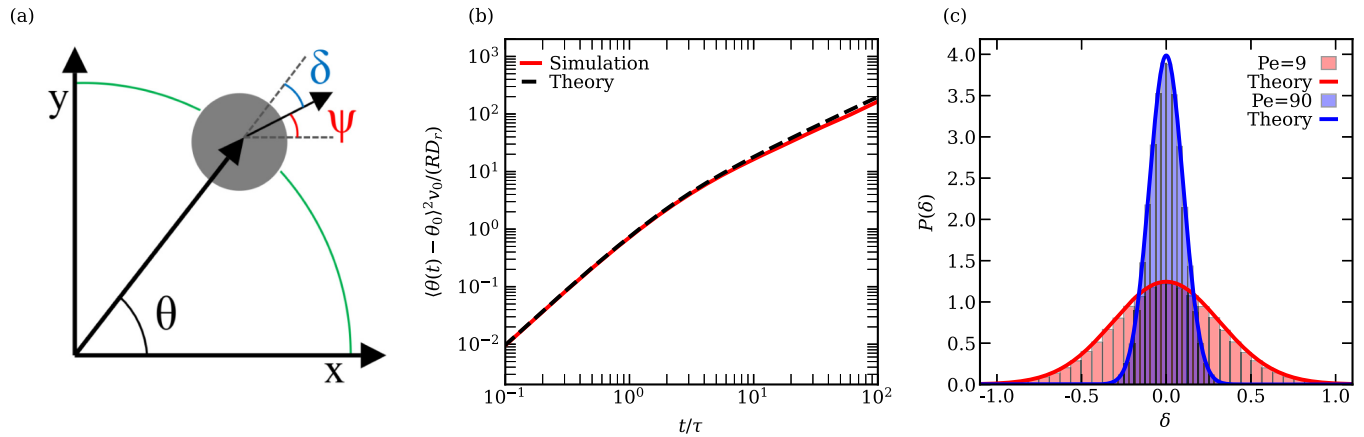


FIG. 1. (a) Schematic diagram of an ABP confined to a ring, whose dynamics can be described by the positional angle θ and the orientational angle ψ . $\delta = \theta - \psi$ is the misalignment angle. (b) Angular MSD of a particle moving on a ring where the ballistic-to-diffusive transition occurs at time $t = \tau = R/v_0$, irrespective of $\tau_r = D_r^{-1}$. (c) Comparison of stationary state distributions $P(\delta)$ from theory and simulations.

demonstrates the reduction of effective particle velocity with increasing Pe as the magnitude of the MSD in the ballistic regime drops. Note that the MSD on a sphere is bounded and therefore the curves saturate for large times.

B. Motility-induced phase separation

We consider an ensemble of N ABPs on a sphere with area packing fraction ϕ , to study how MIPS is affected by the sphere curvature $1/R$. Figure 3 shows the local density distribution (Appendix C) for two different curvatures and corresponding simulation snapshots. The single/double peaks in Fig. 3(a) for the small/large radii $R/\sigma = 16.1$ and $R/\sigma = 26.8$ at the same Péclet number mark the absence/presence of MIPS, respectively. The full phase diagram for different R values is presented in Fig. 4(a). Here, the binodal is constructed by measuring coexisting densities in the phase

separated state, as seen in Fig. 3(a). The spinodal is obtained by computing the particle pressure [46] (Appendix D) as shown in Fig. 5. A sudden drop/change in pressure marks the transition from the homogeneous to the phase-separated state [46–49]. Two main effects of curvature can be seen in Fig. 4(a) for decreasing R : (i) the lower part of binodals and spinodals shifts to larger Pe , and (ii) the two-phase region becomes

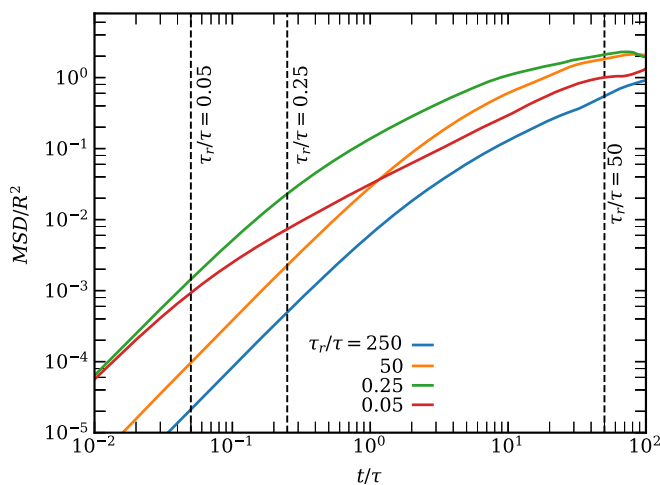


FIG. 2. Positional MSD of a particle moving on a sphere for different τ_r (or Pe), with v_0 fixed. For $\tau_r/\tau < 1$ (green and red curves), the ballistic-to-diffusive transition occurs at time τ_r/τ , whereas for $\tau_r/\tau > 1$ (blue and orange curves), the time scale τ determines the ballistic-to-diffusive transition irrespective of τ_r .

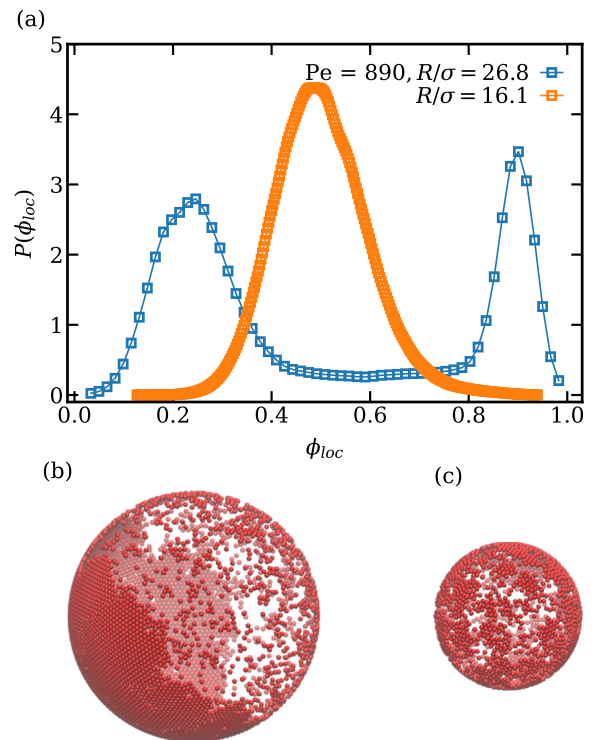


FIG. 3. Curvature-dependent MIPS. (a) Local density distributions for two different radii, indicating the absence of MIPS at large curvatures with $\phi = 0.5$. Simulation snapshots for (b) $R/\sigma = 26.8$, $N = 5760$, and (c) $R/\sigma = 16.1$, $N = 2074$. Parameters are $Pe = 890$ and $\phi = 0.5$. See also movies S1 and S2 in the Supplemental Material [43].

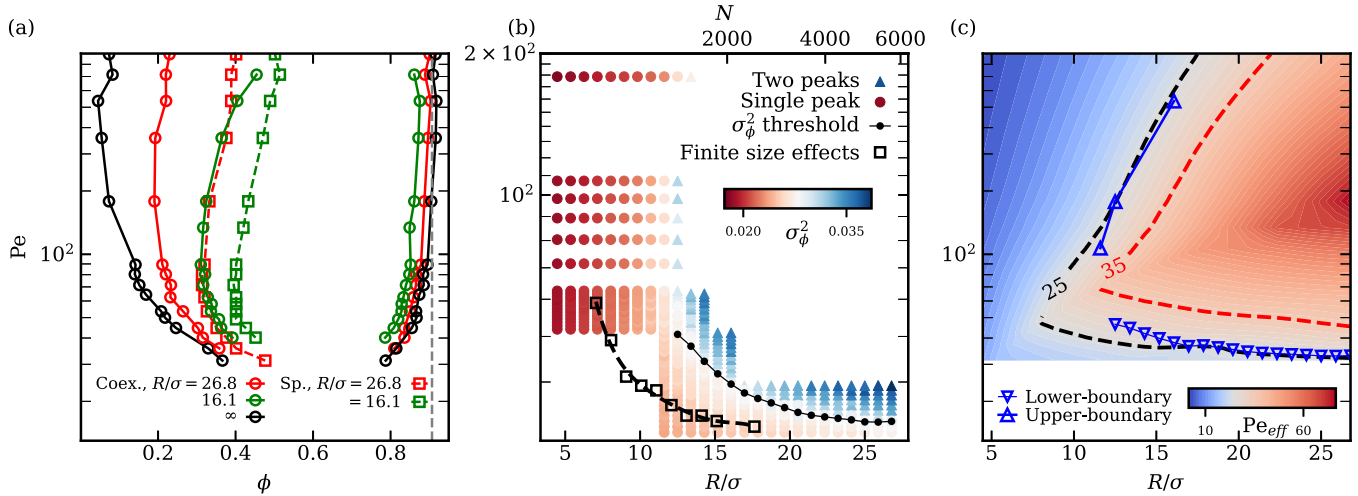


FIG. 4. (a) Pe - ϕ phase diagrams of motility-induced phase separation (MIPS) for three R values. Coexisting densities from the local density distributions (circles) and abrupt pressure drops (squares) are employed to identify the transition. The simulations for determining the coexisting densities are performed for an average area fraction of $\phi = 0.5$. (b) Critical Péclet number $Pe_c(R, 0.5)$ at which MIPS is first observed for increasing Pe at fixed $\phi = 0.5$. The color-bar shows the variance of the local density distribution. Symbols mark the identification of no-MIPS [unimodal $P(\phi_{loc})$] (circles) and MIPS [bimodal $P(\phi_{loc})$] (triangles). The black line with bullets is obtained from the threshold $\sigma_\phi^2 = 0.0305$ of variance of the local density, and it follows well the boundary where the two peaks in the local density distribution merge. The lower x axis shows the changing radius R/σ and the upper curve shows the corresponding number of particles N (for a fixed $\phi = 0.5$). The planar simulations for measuring finite-size effects [squares, $Pe_c(\infty, 0.5)$] is equivalent to the simulations on there sphere by particle number (N) and density $\phi = 0.5$. (c) Heat map of the effective Péclet number Pe_{eff} at the sphere surface as a function of Pe and R . The black and red dashed lines represent $Pe_{eff} = 25$ [i.e., $Pe_{eff} = Pe_c(\infty, 0.5)$] and $Pe_{eff} = 35$, and match well the lower and upper MIPS boundaries from the simulations.

narrower and the slope of the left spinodal/binodal changes sign for large Pe . We denote the phase boundary for different radii as $Pe_c(R, \phi)$, where $R = \infty$ corresponds to the planar case.

Figure 4(b) shows the variation of the critical Péclet number $Pe_c(R, 0.5)$ for a fixed initial density of $\phi = 0.5$. For $R/\sigma \gtrsim 12.5$, MIPS is observed (binodal) with increasing Pe , while for $R/\sigma \lesssim 12.5$, MIPS does not occur. Since the value of R sets the total number N of particles for a fixed ϕ , the phase separation for small R may inherently suffer from finite-size effects (i.e., small N). To separate the effects of curvature and finite system size, planar simulations (Appendix E) for different N with a fixed ϕ are performed, which is not possible for spherical geometries. As particle number decreases, particle out-flux from the dense phase increases with increasing interface curvature, implying higher particle concentrations in the low-density phase [50]. This causes a shift of the spinodals $Pe_c(\infty, \phi)$ upward with decreasing particle number, as seen in Fig. 4(b) for $Pe_c(\infty, 0.5)$. A similar increase in $Pe_c(R, 0.5)$ with decreasing R/σ (and also N) is observed for particles moving on a sphere within the range of $12.5 \lesssim R/\sigma \lesssim 25$. However, the increase in $Pe_c(\infty, 0.5)$ within the range of N corresponding to $12.5 \lesssim R/\sigma \lesssim 25$ is much less pronounced, demonstrating that finite-size effects on the sphere are subdominant. Furthermore, the width of the MIPS region becomes narrower with increasing Pe [see Fig. 4(a)], which explains the sudden disappearance of MIPS at $R/\sigma \approx 12.5$ and $\phi = 0.5$ in Fig. 4(b) (i.e., the spinodal has a turning point before $\phi = 0.5$ is reached for $R/\sigma \lesssim 12.5$). This also supports that the loss of MIPS at $R/\sigma \approx 12.5$ is not due to finite-size effects.

MIPS occurs as a result of slowing down of ABPs due to crowding, which promotes a further reduction in velocity and clustering through a positive feedback mechanism [11,51]. A requirement for MIPS is that the lifetime of small clusters is larger than the persistent travel time of ABPs [22,52]. This means that the directed self-propelled motion should dominate over diffusive motion on the length scale of particle diameter σ , i.e., $\sigma/\tau_r \ll v_0$ or $Pe = v_0\tau_r/\sigma \gg 1$. For ABP motion on a curved surface, this argument has to be modified as follows. First, the propulsion velocity v_0 has to be replaced by a tangential velocity $v_t(R, Pe)$, which depends on R and Pe . In general, $v_t(R, Pe)$ decreases with decreasing R or increasing Pe , e.g., in 2D, $v_t(R, Pe) = v_0(\tau_r/\tau)^{-0.5}$ for $R/Pe < 1$. Figure 6(a) shows the average magnitude of the tangential velocity $v_t(R, Pe) = \langle v_t \rangle$ for a single ABP on a sphere as a function of τ_r/τ (or Pe/R). In qualitative agreement with the two-dimensional results, a power-law decay of the average tangential velocity, i.e., $\langle v_t \rangle \simeq (\tau_r/\tau)^{-\beta}$ is observed, with the exponent β increasing with decreasing radius R , see the inset in Fig. 6(a).

Second, on a curved surface, the time scale τ becomes relevant in addition to τ_r . Thus, we have to distinguish the two cases $\alpha\tau > \tau_r$ and $\alpha\tau < \tau_r$, which represent large and small radii R , respectively. The coefficient α is a weight factor that measures the relative importance of the two time scales. In both cases, the shorter time scale $\tau_{min} = \min(\alpha\tau, \tau_r)$ determines the dynamics. As a result, we can define an effective Péclet number

$$Pe_{eff} = v_t(R, Pe)\tau_{min}/\sigma, \quad (7)$$

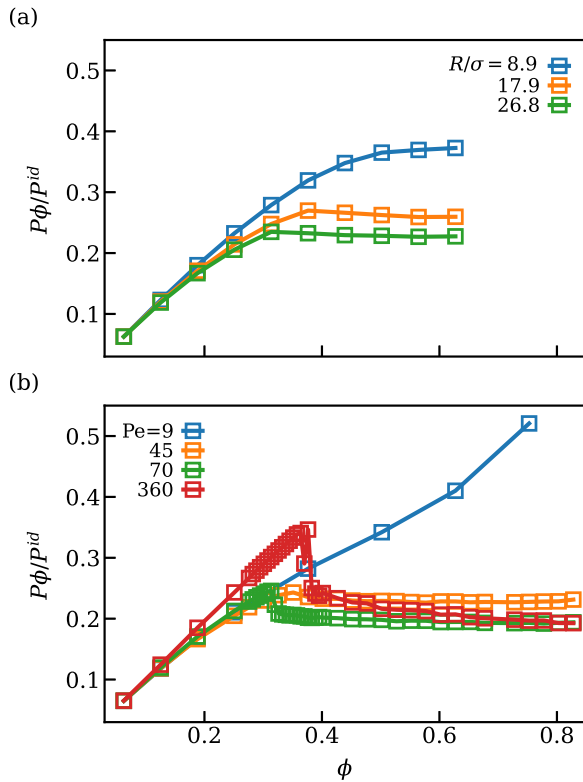


FIG. 5. Pressure P as a function of surface density ϕ (a) for various R at a fixed $Pe = 45$, and (b) for various Pe at a fixed $R/\sigma = 26.8$. P^{id} is the pressure in the absence of interparticle interactions. The effect of decreasing R is qualitatively similar to that of decreasing Pe . At the MIPS transition, a sudden drop in pressure occurs, which is more pronounced at large Pe . For large Pe , the ϕ value at the pressure drop increases, in agreement with local density measurements.

and the variation of the phase boundary can be described by the relation $Pe_{eff}(Pe_c(R, \phi)) = Pe_c(\infty, \phi)$, i.e., for a fixed ϕ , the phase boundary shifts along the contour $Pe_{eff} = Pe_c(\infty)$.

From this argument, all the trends observed in Fig. 4 can be understood. With decreasing R , $Pe_c(R, 0.5)$ first increases, because τ_r is the relevant time scale and $v_t(R, Pe)$ decreases, which has to be compensated by a larger Pe (or τ_r). Note that Pe_{eff} increases with increasing τ_r only as long as $\tau_r < \alpha\tau$. When $\tau_r = \alpha\tau$, Pe_{eff} reaches a maximum as a function of Pe for a fixed R . A further increase in Pe only causes a decrease in the tangential velocity $v_t(R, Pe)$, without any increase in $\tau_{min} = \alpha\tau$. This leads to a decrease in Pe_{eff} and the turning of the low- ϕ branch of two-phase coexistence toward larger ϕ values in Fig. 4(a).

At low-to-intermediate particle densities ($\phi < 0.5$) and small radii $R \lesssim 12.5$, with $\tau_r > \alpha\tau$, MIPS is absent for all Pe . This inversion of time scales and disappearance of MIPS occur when particle diffusion dominates over the minimum run length for cluster formation. In this case, an increase of τ_r cannot lead to MIPS, because the slowing down of translational ABP motion on a curved surface always precedes rotational diffusion.

Figure 4(c) shows a heat map of Pe_{eff} for various radii, where $\alpha = 6$ is selected for a good fit of the simulation data

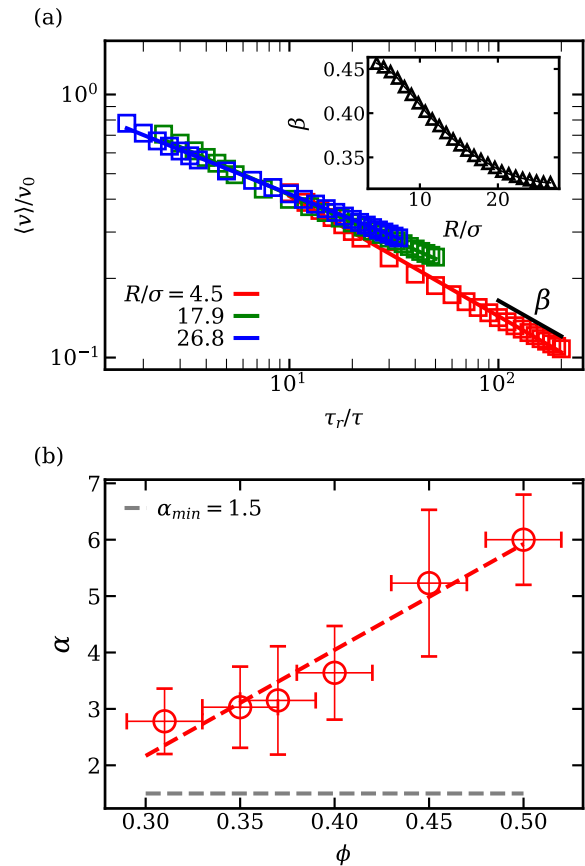


FIG. 6. (a) Normalized average tangential velocity $\langle v_t \rangle / v_0$ as a function of τ_r / τ for different radii exhibiting a power-law decay $\langle v_t \rangle / v_0 \sim (\tau_r / \tau)^{-\beta}$. The inset shows the value of β extracted for different radii R , suggesting a stronger decay for large sphere curvatures. (b) Weight factor α as a function of surface density ϕ . The gray dashed line is the minimum value of α estimated for a free particle.

for MIPS (a more detailed discussion on α is provided later in the text). Lower and upper boundaries of the MIPS region for a fixed $\phi = 0.5$ agree well with the line $Pe_{eff} = Pe_c(\infty, 0.5)$. Furthermore, the heat map of Pe_{eff} nicely explains the loss of MIPS at small R . Figure 4(c) also shows that for a smaller ϕ [i.e., a larger critical $Pe_{eff} = Pe_c(\infty, \phi < 0.5)$], the MIPS regime becomes narrower as a function of R , consistent with the onset of MIPS at larger ϕ for decreasing R . Noteworthy, for a fixed R , Pe_{eff} reaches a maximum and then decreases as a function of Pe , which explains the turning of the phase boundary at large Pe . This supports the existence of a reentrant behavior (i.e., from homogeneous to MIPS and back to homogeneous density) with increasing Pe for a wide range of radii.

From the phase diagram in Fig. 4(a), α is determined by the relation $\alpha(\phi) = \langle v_t \rangle_l Pe_l \sigma / \langle v_t \rangle_u R$, where the indices l and u correspond to the lower and upper branches of the spinodal respectively and we have equated $Pe_{eff,l} = Pe_{eff,u}$. Figure 6(b) shows that α increases with increasing surface area fraction ϕ . In the dilute limit, the value of α can be estimated by fitting the MSD curve of an ABP on a sphere in the limit $\tau_r / \tau \gg 1$ with the solution for the planar case [53] [with a reduced velocity $v \simeq v_0(\tau_r / \tau)^{-\beta}$] to get $\alpha = 1.5$. With increasing ϕ ,

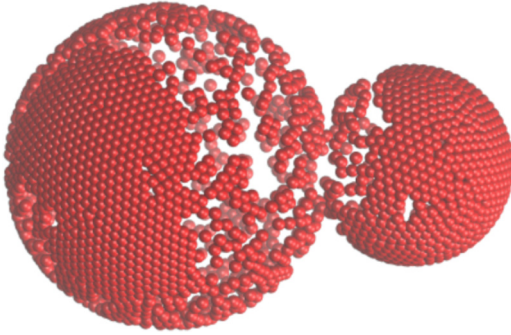


FIG. 7. Two connected pores with different radii $R_1/\sigma = 16.1$ and $R_2 = 0.6R_1$, connected by a passage of radius $R_p = 3.2\sigma$ with $N = 2500$ at $Pe = 90$ (see also movie S3 [43]).

interparticle collisions become relevant, so that the particle dynamics is significantly affected and the simple estimate based on single-particle α is not valid, thus leading to shift of α with ϕ . The increase in the value of α with ϕ explains why a significant change in the right binodal/spinodal at large ϕ with curvature is not observed.

C. Two spherical pores connected by a small passage

Next, we make a further step toward the understanding of the behavior of ABPs at curved surface with complex geometries. Confinement strongly affects transport in active-matter systems, and leads to a plethora of new behaviors, such as robust swimming of bacteria under strong confinement [54], development of self-sustained density oscillations in a system of microchambers connected via a narrow channel [55], and different transport properties of motile and nonmotile bacteria in porous media [28].

As a paradigmatic example for complex geometries and porous media, we consider two spherical pores with unequal radii, which are connected by a small passage of radius R_p , as shown in Fig. 7. The setup consists of two confining spheres of radii $R_1 + 2^{1/6}\sigma/2$ and $R_2 + 2^{1/6}\sigma/2$, with their centers at $(-R_1, 0, 0)$ and $(R_2 - \Delta, 0, 0)$, respectively, where Δ is the overlap of the two spheres along the line connecting their centers. These particles interact with the spheres via the LJ potential (3) with a minima at a distance R_1 and R_2 . The interaction is cut off at a distance $r = \sigma$ from the sphere so that only up to a single layer of ABPs is attracted towards the spherical walls. At the intersection of the two outer sphere surfaces, a ring of particles, which interact with the ABPs via the repulsive LJ potential is placed, to prevent the escape of ABPs near the passage. The system is initiated with a homogeneous (equilibrium) ABP distribution on both spherical surfaces. Simulations are performed for varying particle numbers and activity. Note that in this setup, there can be more than one layer of SPPs on the sphere surface as there is no inner sphere constraining the particles to the wall; however, the formation of multiple layers is not observed in the simulations reported below. We consider two connected pores with radii $R_1/\sigma = 16.1$, $R_2/R_1 = 0.6$, and a passage sizes $R_p = 3.2\sigma$ and $R_p = 3 = 6.2\sigma$.

In the absence of excluded volume effects, theoretical results for particles with spatially varying velocities predict the

single-particle density to be proportional to the inverse of the particle velocity, i.e. $\phi(\mathbf{x}) \sim 1/v(\mathbf{x})$, for a surface with a coordinate system \mathbf{x} [41,42]. Since the particles have different velocities in the two pores, we therefore expect $\phi_1 v_{t1} = \phi_2 v_{t2}$, where v_{t1} and v_{t2} are the tangential velocities of the ABPs in the two spheres in the dilute limit. Here $\phi_i = N_i A_\sigma / A_i$ for each pore $i = 1, 2$, where N_i is the particle number, A_i is the area of the pore, and $A_\sigma = \pi\sigma^2/4$ is the area occupied by an ABP, which is approximated to be equal to its value on a flat surface. Figure 8(a) shows the product of $\phi_1 v_{t1}$ vs $\phi_2 v_{t2}$, for varying N with fixed Pe (circles) and varying Pe with fixed N (squares). We find that the agreement with the theory (i.e., the diagonal) is good for low N and/or high Pe . As N is increased, excluded volume effects become more significant, causing the deviation from theory. Similarly, phase separation within either of the two pores invalidates the relation, as the local density near the passage becomes lower than the average density in the pore. Moreover, at lower Pe , particles have larger tangential velocities, implying a higher effective pressure and an increased prevalence of interactions between ABPs.

The simple relation $\phi(\mathbf{x}) \sim K(\mathbf{x})$ for a surface with a local (Gaussian) curvature $K(\mathbf{x})$ no longer holds in our system (cf. Fig. 11 Appendix F) due to the presence of a non-convex boundary at the passage between the pores [34,35]. The validity of $\phi(\mathbf{x}) \sim 1/v(\mathbf{x})$ can be understood as arising by the gliding motion of the particles at the passage, with different velocities on either side.

Our results in Fig. 4(a) for MIPS in a single pore facilitate the interpretation and understanding of the steady-state behavior of ABPs in the two pores. As N is increased for a given Pe , the particles in either sphere can phase separate only when their surface density exceeds $\phi_c(R, Pe)$ for MIPS. Due to lower velocities in the smaller pore, it is expected to fill first and phase separate for $\phi_2 > \phi_c(R_2, Pe)$. The number density of particles in the small pore cannot exceed the close-packing density ϕ_{cp} . Combining this with the equations $\phi_1 v_{t1} = \phi_2 v_{t2}$ and $\phi_1 A_1 + \phi_2 A_2 = N$, we get $\phi_2(N) = \min(N[A_2 + A_1 v_{t2}/v_{t1}]^{-1}, \phi_{cp})$. Similarly, the particles in the larger pore will phase separate for the N , which satisfies $\phi_1 > \phi_c(R_1, Pe)$, where $\phi_1 = \phi_2(N) v_{t2}/v_{t1}$. From the single-pore results in Fig. 4(a), MIPS in the larger pore is expected at $\phi_1 \simeq 0.4$ and $\phi_1 \simeq 0.5$ for $Pe = 90$ and $Pe = 890$, respectively. This corresponds to the values $N \gtrsim 2300$ and $N \gtrsim 2900$, and is confirmed by the simulation results in Fig. 8(b), where the onset of phase separation as a function of N is characterized by a sudden rise in the fraction n_{cl} of particles occupying clusters of size greater than $N_1/2$. Note that the reduction of the effective Péclet number at large Pe implies that a larger N is required for MIPS. An increase in the passage radius R_p would result in a decrease in the required N for phase separation due to a reduction in the pore areas A_1 and A_2 . For a passage radius $R_p = 6.2\sigma$, MIPS is predicted to occur at $N \gtrsim 2200$ and $N \gtrsim 2800$ for $Pe = 90$ and $Pe = 890$, respectively. The shift due to increasing passage radius can nicely be seen in Fig. 8(b), where $n_{cl} \gtrsim 0.7$ is considered as an indicator for a stable phase-separated state.

It is also interesting to study the steady-state number fluxes F_{12} and F_{21} through the passage leaving and entering the large pore, respectively (i.e., the number of particles per unit time and circumference). This is related to more general questions

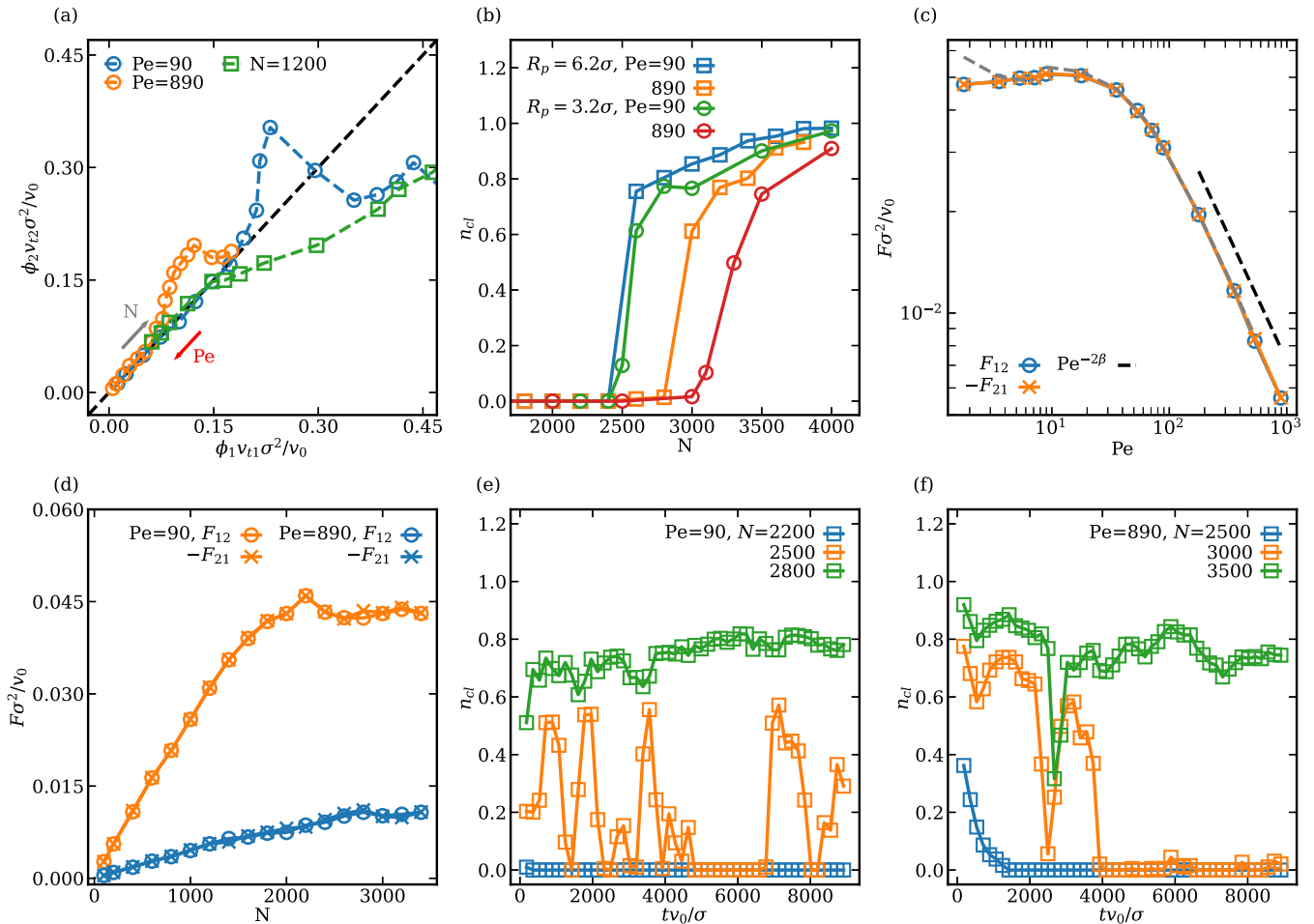


FIG. 8. (a) Plot of $\phi_1 v_{t1}$ vs $\phi_2 v_{t2}$, for varying N with fixed Pe (circles) and varying Pe with fixed N (squares) for $R_p = 6.2\sigma$. (b) Fraction n_{cl} of particles in the large sphere occupying clusters of size larger than $N/2$ as a function of N for different Pe and passage size R_p . The sudden jump identifies a MIPS transition. Number fluxes F_{12} , F_{21} , and F_{total} as a function (c) of Pe for fixed $N = 1200$, and (d) of N for fixed Pe , with passage size $R_p = 6.2\sigma$. F_{12} is the flux from pore 1 to 2 and the black dashed line in (c) indicates the power law $Pe^{-2\beta}$, where $\beta = [\beta(R_1/\sigma) + \beta(R_2/\sigma)]/2$. The gray dashed line is the flux obtained by varying Pe via v_0 (i.e., propulsion force), with a fixed $\tau_r = 100$ and $\gamma = 10$. For $Pe < 1000$, $\sigma/v_0 \gg \tau_{relax}$ ensuring the over-damped limit and the choice $\epsilon = f_p \sigma$ ensures a fixed ABP diameter even for large activities. Fraction n_{cl} of particles in large clusters as a function of time for (e) $Pe = 90$ and (f) $Pe = 890$, with $R_p = 3.2\sigma$.

of the escape of active particles from geometrical confinement [56,57]. The simulation results for the flux, displayed in Figs. 8(c), 8(d) show that the total steady-state flux $F_{total} = F_{12} + F_{21}$ vanishes, as it should.

For large Pe values (>100), the relation $\phi_1 v_{t1} = \phi_2 v_{t2}$ applies [Fig. 8(a)], and therefore $\phi_2 > \phi_1$, due to a lower tangential velocity in the small sphere. At the same time, there is a significant nonzero flux F_{12} from the large to the small pore, such that ABPs move against the density gradient. The spatially varying velocity of particles (i.e., between the two pores) leads to a drift of the particles toward regions of lower mobility [42]. Thus, two competing mechanisms contribute to the flux in this system, one arising from the diffusion of the particles due to the concentration gradient and the other due to their spatially varying mobility. Both of these (dimensionless) fluxes are proportional to the ratio v_t^2/τ_{min} [42]. At large Pe , τ_{min} saturates, so that the flux can be expected to vary as $F \sim v_t^2 \sim Pe^{-2\beta}$ [Fig. 6(a)]. Choosing the mean value of $\beta = [\beta(R_1/\sigma) + \beta(R_2/\sigma)]/2$ as the exponent, we obtain a good agreement with the data, as seen in Fig. 8(c). Notably,

it is the Péclet number that controls the (dimensionless) flux and not the particle velocity. We confirm this by varying Pe via v_0 instead of τ_r and observe a universal scaling with Pe . It is important to note that in the regime of low Pe , we observe $\phi_1 > \phi_2$, and so both diffusive and drift fluxes are expected to favor accumulation in the smaller sphere. However, the results in Fig. 8(c) suggest that the flux is balanced by particle motion from the small sphere to the large sphere, whose physical origin remains to be clarified. Considering that we observe a plateau of the flux at low Pe , it is possible that the flux is mainly thermal in nature. Note that the plateau arises because the flux in Fig. 8(c) is normalized by the velocity v_0 , which implies that the flux decreases linearly with decreasing Pe .

At fixed Pe , the particle flux grows linearly with particle number N , as shown in Fig. 8(d). However, phase separation in the smaller pore causes a sudden drop in the density near the passage, leading to a reduction in the particle flux, see Fig. 8(d) for $N \simeq 2000$, $Pe = 90$. The deviation from linear growth is less pronounced at higher Pe , as the binodals curve inward at large Pe , implying a smaller difference between the

mean density and the gas-phase density in the phase-separated state. The larger tangential mobility of the particles at $Pe = 90$ leads to higher magnitude of the individual fluxes F_{12} and F_{21} .

Another interesting behavior is the temporal evolution of the system starting from an initial uniform equilibrium distribution of ABPs near the MIPS transition. For $\phi_1 \simeq \phi_c(R_1, Pe)$, the larger pore shows a dynamic MIPS state, as seen in Figs. 8(e), 8(f) for $N = 2500$ ($Pe = 90$) and $N = 3000$ ($Pe = 890$). For the higher $Pe = 890$, there is an initial MIPS state in the larger sphere at small times followed by the disappearance of MIPS at longer times $t v_0/\sigma > 4000$, see Fig. 8(f). This occurs because the larger sphere starts out with a sufficient number of particles for phase separation, but with time, loses particles to the smaller sphere as the system relaxes to the steady state. In contrast, for lower $Pe = 90$, fluctuations in particle number within the different pores become important in the transition regime, and can lead to dynamic restoration and loss of MIPS, see Fig. 8(e), where strong fluctuations in n_{cl} are present. Note that the fluctuations of ABP numbers within the different pores are larger at a lower Pe , which is consistent with the absence of intermittent MIPS at $Pe = 890$.

IV. SUMMARY AND CONCLUSIONS

We have studied the dynamics and phase behavior of ABPs on curved surfaces and in porous media. When the propulsion direction of ABPs can vary diffusively in 3D (i.e., it is not aligned with the local tangent plane of the surface), the behavior of active particles on curved surfaces is very different compared to ABPs with propulsion direction confined to a plane. Nonzero curvature results in a stop-and-go motion, such that particles slide along the surface when their orientation is different from the local surface normal, and then stop after their orientation becomes perpendicular to the surface. This behavior governs motility-induced phase separation on curved surfaces, e.g., the MIPS region rapidly shrinks with increasing curvature and eventually disappears. Furthermore, curved surfaces lead to a possible reentrant behavior, where MIPS for a fixed surface density of ABPs first appears with increasing Pe , and then can disappear. This behavior should not be confused with the reentrant behavior in 2D observed for soft interaction potentials, where the effective particle diameter (and thus packing fraction) is reduced with increasing propulsion strength.

Our results for the two-pore system suggest that particle exchange between the pores depends strongly on the pore curvatures and MIPS within the pores. The mean density in a pore is found to be proportional to its inverse tangential velocity only for large Péclet numbers. Moreover, MIPS in either pore leads to different local densities near the entrance of the passage, causing a reduction in the directional flux between the two pores. Such a system is also capable of showing transient MIPS phases, due to fluctuations of particle numbers that drive it in and out of the MIPS state. We also find that the (dimensionless) particle flux is inversely proportional to Péclet number.

We hope that our work will contribute to a better understanding of a variety of issues related to the behavior of active particles at curved surfaces, such as the preferred occupation of certain geometries and niches by bacterial colonies [58], the

behavior of microbial communities in complex environments such as porous rocks [59] and water droplets [60], and the self-jamming on microbes growing in complex environments [61,62].

While we have presented a comprehensive picture of the effect of curvature on phase separation and particle dynamics in single and connected pores, our study is by no means exhaustive. Further work needs to be done for understanding the effective Péclet number and the relevance of the parameter α in its definition. A theoretical approach using mean-field approximations may provide a proper definition of the effective Péclet number and how it modifies the resulting phase diagram, particularly the asymmetry between the high- ϕ and low- ϕ branches. In the two-pore system, at low Pe , there is a counteracting flux from the small to the large sphere that balances the incoming flux, despite the higher particle density and mobility in the larger sphere. The origin of this flux needs further study. Furthermore, it would be very interesting to take hydrodynamic interactions between particles into account, which should lead to significantly different behaviors depending on the type of propulsion of a microswimmer.

APPENDIX A: ANALYTICAL SOLUTION OF THE LANGEVIN EQUATION FOR AN ABP ON A RING

The equation of motion for an active Brownian particle (ABP) with a position vector $\mathbf{r} = R(\cos \theta, \sin \theta)$, orientation vector $\mathbf{e} = (\cos \psi, \sin \psi)$, confined to move on a ring with radius R in 2D, is given by

$$\dot{\mathbf{r}} = v_0(\mathbf{e} \cdot \mathbf{e}_\theta)\mathbf{e}_\theta, \quad \dot{\theta} = -\frac{v_0}{R} \sin(\theta - \psi), \quad \dot{\psi} = \sqrt{2D_r}\Gamma_\psi, \quad (\text{A1})$$

where v_0 is the ABP propulsion velocity, $\mathbf{e}_\theta = \mathbf{r}/R$, D_r is the rotational diffusion, and Γ_ψ is the rotational noise with $\langle \Gamma_\psi \rangle = 0$ and $\langle \Gamma_\psi(t)\Gamma_\psi(t') \rangle = \delta(t - t')$. After the linearization of these equations in the limit of large Pe (i.e., small misalignment angle $|\delta| \equiv |\theta - \psi| \ll 1$) and normalization of time by $\tau = R/v_0$, we obtain the dimensionless equations

$$\dot{\theta} = -\theta + \psi, \quad \dot{\psi} = \tau\sqrt{2D_r}\Gamma_\psi, \quad (\text{A2})$$

$$\ddot{\theta} = -\dot{\theta} + \tau\sqrt{2D_r}\Gamma_\psi. \quad (\text{A3})$$

The Fokker-Plank equation for $\dot{\theta}$ is given by

$$\frac{\partial}{\partial t^*} P(\dot{\theta}, t^*) = \frac{\partial}{\partial \dot{\theta}} (\dot{\theta} P(\dot{\theta}, t^*)) + D_r \tau \frac{\partial^2}{\partial \dot{\theta}^2} P(\dot{\theta}, t^*), \quad (\text{A4})$$

where t^* denotes the dimensionless time. In the stationary state, we obtain

$$P(\dot{\theta}) = \frac{1}{\sqrt{2\pi D_r \tau}} \exp\left[\frac{-\dot{\theta}^2}{2D_r \tau}\right], \quad \langle \dot{\theta}^2 \rangle = D_r \tau. \quad (\text{A5})$$

Integration of Eq. (A3) leads to

$$\begin{aligned} \dot{\theta}(t^*) &= \dot{\theta}(0)e^{-t^*} + \tau e^{-t^*} \int_0^{t^*} \sqrt{2D_r}\Gamma_\psi(s)e^s ds, \\ \langle \dot{\theta}(t_1^*)\dot{\theta}(t_2^*) \rangle &= \dot{\theta}^2(0)e^{-(t_1^*+t_2^*)} + \tau D_r [e^{-|t_1^*-t_2^*|} - e^{-(t_1^*+t_2^*)}]. \end{aligned} \quad (\text{A6})$$

Then, the angular mean-squared displacement (MSD) can be calculated using $\theta(t^*) - \theta(0) = \int_0^{t^*} \dot{\theta}(s) ds$, and is given by

$$\begin{aligned} \langle (\theta(t^*) - \theta(0))^2 \rangle &= \int_0^{t^*} \int_0^{t^*} \langle \dot{\theta}(s') \dot{\theta}(s) \rangle ds ds' \\ &= (\dot{\theta}^2(0) - \tau D_r)(1 - e^{-t^*})^2 + 2\tau D_r t^* \\ &\quad - 2(1 - e^{-t^*})\tau D_r. \end{aligned} \quad (\text{A7})$$

Finally, using the result $\langle \dot{\theta}^2 \rangle = \tau D_r$ from Eq. (A5), we obtain

$$\langle (\theta(t^*) - \theta(0))^2 \rangle = 2\tau D_r t^* - 2(1 - e^{-t^*})\tau D_r. \quad (\text{A8})$$

MSD in the dimensional form becomes

$$\langle (\theta(t) - \theta(0))^2 \rangle = 2D_r t - 2\tau D_r [1 - \exp(t/\tau)], \quad (\text{A9})$$

and in the limit of small and large times, MSD is given by

$$\langle (\theta(t) - \theta(0))^2 \rangle = \begin{cases} (\tau_r \tau)^{-1} t^2, & t \rightarrow 0, \\ 2D_r t, & t \rightarrow \infty, \end{cases} \quad (\text{A10})$$

where $\tau_r = D_r^{-1}$ is the rotational diffusion time and $\langle \dot{\theta}^2 \rangle = (\tau_r \tau)^{-1}$. Therefore, the transition from ballistic to diffusive motion takes place at $t \sim \tau$, suggesting that for large curvatures (or small R), the particle moves ballistically for times shorter than $\tau = R/v_0$.

For the misalignment angle $\delta = \theta - \psi$, we have the dimensionless equation

$$\dot{\delta} = -\sin \delta + \tau \sqrt{2D_r} \Gamma_\psi, \quad (\text{A11})$$

with the corresponding Fokker-Planck equation

$$\frac{\partial}{\partial t^*} P(\delta, t^*) = \frac{\partial}{\partial \delta} [(\sin \delta) P(\delta, t^*)] + \tau D_r \frac{\partial^2}{\partial \delta^2} P(\delta, t^*). \quad (\text{A12})$$

Equation (A12) can be solved to obtain the stationary-state distribution

$$P(\delta) = \frac{1}{2\pi I_0(\tau_r/\tau)} \exp\left[\frac{\cos \delta}{\tau D_r}\right], \quad (\text{A13})$$

where $I_0(\tau_r/\tau)$ is the modified Bessel function of the first kind. In the limit $|\delta| \ll 1$, $\dot{\theta} = \delta$, and the resulting distributions for δ and $\dot{\theta}$ are identical and given in Eq. (A5). In the limit $|\delta| \ll 1$, the dimensional tangential velocity $v = v_0 \sin \delta$ becomes

$$\sqrt{\langle v^2 \rangle} = v_0 \sqrt{\tau/\tau_r}, \quad (\text{A14})$$

where we have used that $\langle \delta^2 \rangle = \tau/\tau_r$. Thus, the particle tangential velocity decreases with both increasing activity (equivalently increasing τ_r) and increasing curvature (or decreasing τ).

APPENDIX B: RADIAL DISTRIBUTION FUNCTION

Radial distribution function (RDF) of the particles is plotted in Fig. 9 for different Pe at $R/\sigma = 16.1$ in the phase-separated state to check whether there is any change in the effective particle radii. RDFs for different Pe show no visible change in the peak positions, supporting that simulations do not suffer from any possible artifacts due to the softness of

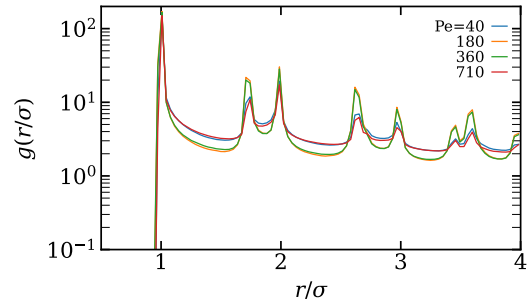


FIG. 9. Radial distribution function (RDF) of particles for different Pe at $R/\sigma = 16.1$. Location of the peaks is nearly independent of Pe, suggesting that the effective density is not altered. Moreover, the RDF for Pe = 40 is similar to that for Pe = 710, consistent with the observation of the turning of the phase diagram at large Pe.

the particles. Therefore, the choice of ABP diameter as $\sigma = 2^{1/6}\sigma_{LJ}$ is well justified. Note that the peaks in RDF broaden for large Pe, suggesting that the effective Péclet number Pe_{eff} on the sphere decreases at large Pe.

APPENDIX C: LOCAL DENSITY MEASUREMENTS

Two different methods are employed for local density measurements: (i) direct sampling of local density, and (ii) the construction of a Voronoi diagram. In the first method, a sampling grid of N_s points is considered, and the local density for each sampling point j at the position \mathbf{s}_j is calculated as

$$\phi_{\text{loc},j} = \pi \sigma^2 \frac{n_j^p}{4A_{\text{loc}}}, \quad (\text{C1})$$

where n_j^p is the number of ABPs within the cutoff distance $r_{\text{cut}} = 4.5\sigma$ from the position \mathbf{s}_j and $A_{\text{loc}} = \pi r_{\text{cut}}^2$ is the local area around each sampling point. This method is used for determining the coexisting densities in the phase-separated state, as a uniform placement of sampling points ensures that the two peaks in local density are well separated and can easily be localized.

The second method involves the construction of a Voronoi diagram given the particle positions as the generating points. After the Voronoi diagram is built, the area A_i of each Voronoi cell associated with a particle i is used to determine the local area as

$$\phi_{\text{loc},i} = \pi \sigma^2 / (4A_i). \quad (\text{C2})$$

In this method, the peak in local density representing the gas phase is low in intensity and broad due to a large variation in polygon areas for the low-density state. On the other hand, the high-density phase often exhibits multiple peaks, corresponding to variations in local ordering in the large MIPS cluster (locally crystalline, locally hexatic, and locally liquid). However, these local variations do not give a proper measure of the average local density in the MIPS cluster. This is why the local sampling method is used for the determination of coexisting densities. However, the Voronoi analysis can be performed much faster and does not depend on the choice of the cutoff distance r_{cut} , whose selection becomes increasingly harder as the system size decreases for decreasing R . As a

result, both methods are employed in the analysis of MIPS, as they show the shift from unimodal to bimodal distribution of local density near the same (critical) Pe .

APPENDIX D: PRESSURE MEASUREMENTS

Pressure in the simulated system is calculated using the virial theorem [48,49,63], which states that for a confined system of N particles in the overdamped limit, we have

$$\sum_{i=1}^N \langle \mathbf{F}_i(t) \cdot \mathbf{r}_i(t) \rangle = 0, \quad (\text{D1})$$

where $\mathbf{F}_i(t)$ is the total force acting on particle i . Equation (D1) is expanded by considering different forces present in the simulated system as

$$\begin{aligned} \sum_{i=1}^N \langle f_p e_i(t) \cdot \mathbf{r}_i(t) \rangle + \frac{1}{2} \sum_{i=1}^N \sum_{j=1}^N \langle \mathbf{F}_{i,j}(t) \cdot (\mathbf{r}_i(t) - \mathbf{r}_j(t)) \rangle \\ + \sum_{i=1}^N \langle \mathbf{F}_{i,\text{conf}}(t) \cdot \mathbf{r}_i(t) \rangle = 0, \end{aligned} \quad (\text{D2})$$

where $\mathbf{F}_{i,\text{conf}}(t)$ is the confinement force on particle i , and $\mathbf{F}_{i,j}(t)$ is the inter-ABP force between particles i and j . Now, the internal virial V_{int} due to internal forces and the external virial V_{ext} due to forces from the confining potential can be defined as

$$\begin{aligned} V_{\text{int}} &= \sum_{i=1}^N \langle f_p e_i(t) \cdot \mathbf{r}_i(t) \rangle + \frac{1}{2} \sum_{i=1}^N \sum_{j=1}^N \langle \mathbf{F}_{i,j}(t) \cdot (\mathbf{r}_i(t) - \mathbf{r}_j(t)) \rangle, \\ V_{\text{ext}} &= \sum_{i=1}^N \langle \mathbf{F}_{i,\text{conf}}(t) \cdot \mathbf{r}_i(t) \rangle, \end{aligned} \quad (\text{D3})$$

where $V_{\text{ext}} = -V_{\text{int}}$. Then, the pressure in the system is related to the internal virial as

$$3pV \simeq V_{\text{ext}} = -V_{\text{int}}, \quad (\text{D4})$$

where $V = 4\pi R^2 \sigma$. Thus, the pressure can be calculated using either the internal or external virial. In our simulation setup, the particles continuously interact with the confining wall, and therefore, even V_{ext} gives a good estimate of the system pressure due to sufficient averaging. We have verified the equality $V_{\text{ext}} = -V_{\text{int}}$ for a few simulations. To compute pressure, the external virial is used for all simulations, as the computational cost of the external virial scales as $\sim N$, whereas for the internal virial, it scales as $\sim N^2$.

APPENDIX E: PLANAR SIMULATIONS

To study the finite-size effects due to a finite number N of particles for a spherical confinement, we also perform simulations of ABPs moving in a planar (slitlike) geometry. This is achieved by confining the particles to the x - y plane using two planar surfaces placed at $z = \sigma_{LJ}/2$ and $z = -\sigma_{LJ}/2$, at which the LJ potential is applied. In the x and y directions, periodic boundary conditions are employed. The simulation domain corresponds to a square with a side length L , where the surface density of ABPs is given by

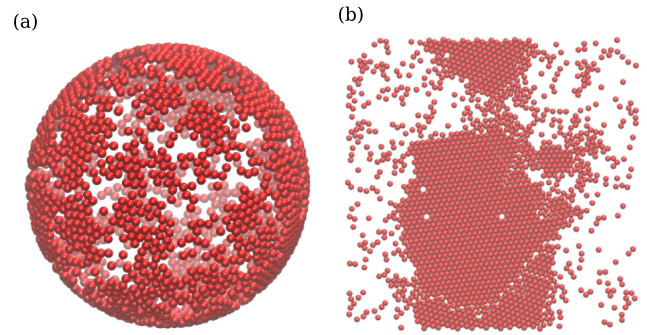


FIG. 10. Simulation snapshots for a fixed $Pe = 890$ and $\phi = 0.5$. (a) Spherical geometry with $R/\sigma = 16.1$ and $N = 2074$, and (b) planar confinement ($R = \infty$) with $N = 1834$. The two systems have nearly same number of particles, indicating that the absence of MIPS for $R/\sigma = 16.1$ is not predominantly due to finite-size effects.

$\phi = N\pi\sigma^2/(4L^2)$. The corresponding simulation on a sphere has the same N and ϕ with a sphere radius of $R/\sigma = L/(2\sqrt{\pi}\sigma)$.

Finite-size effects lead to a shift of the critical Péclet number Pe_c for motility-induced phase separation (MIPS) toward larger Pe values for decreasing L (or R), see Fig. 4(b). Thus, the boundary for MIPS in Fig. 4(b) representing Pe_c as a function of R is corrected for finite-size effects measured in the planar simulations. Furthermore, to compare the effective Péclet number Pe_{eff} on a sphere with that for the planar case, we also compute the planar Péclet number Pe_{pl} based on the average mean-squared planar velocity v , i.e., $Pe_{pl} = Pe\sqrt{\langle v^2 \rangle}/v_0$. For example, MIPS for $\phi = 0.5$ is first observed at $Pe = 31$, which corresponds to $Pe_{pl} \simeq 25$.

Figure 10 shows the simulation snapshots of ABPs on a sphere with radius $R/\sigma = 16.1$ and confined to a plane ($R = \infty$) at $Pe = 890$. Both simulations have nearly same number of particles, however, MIPS is not observed on the sphere, indicating that the absence of MIPS for small spheres is indeed a curvature effect.

APPENDIX F: PORE DENSITY

Figure 11 shows the product ϕR^2 of the density and the inverse local Gaussian curvature (R^2) for the two-pore system

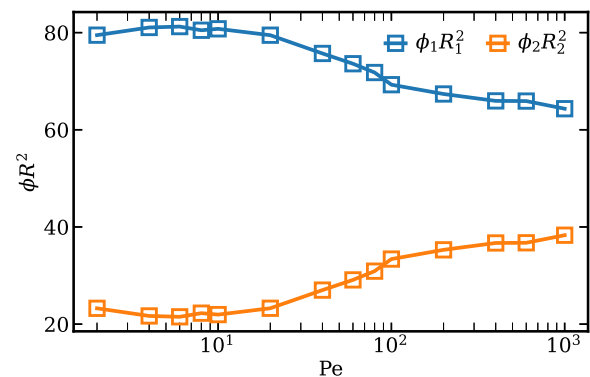


FIG. 11. ϕR^2 as a function of Pe for the two-pore system at a fixed $N = 1200$, indices 1 and 2 correspond to the two pores.

as a function of Pe . It is clear that the simple relation $\phi \sim 1/R^2$ for large Pe , does not hold for this system, as $\phi_1 R_1^2 \neq \phi_2 R_2^2$.

This is due to the presence of the nonconvex boundary at the passage connecting the two systems.

-
- [1] J. Elgeti, R. G. Winkler, and G. Gompper, Physics of microswimmers—single particle motion and collective behavior: a review, *Rep. Prog. Phys.* **78**, 056601 (2015).
- [2] C. Bechinger, R. Di Leonardo, H. Löwen, C. Reichhardt, G. Volpe, and G. Volpe, Active Brownian particles in complex and crowded environments, *Rev. Mod. Phys.* **88**, 045006 (2016).
- [3] G. Gompper, R. G. Winkler, T. Speck, A. Solon, C. Nardini, F. Peruani, H. Löwen, R. Golestanian, U. B. Kaupp, L. Alvarez, T. Kioerboe, E. Lauga, W. Poon, A. D. Simone, F. Cichos, A. Fischer, S. M. Landin, N. Söker, R. Kapral, P. Gaspard *et al.*, The 2020 motile active matter roadmap, *J. Phys.: Condens. Matter* **32**, 193001 (2020).
- [4] Y. Fily and M. C. Marchetti, Athermal Phase Separation of Self-Propelled Particles with No Alignment, *Phys. Rev. Lett.* **108**, 235702 (2012).
- [5] J. Bialké, H. Löwen, and T. Speck, Microscopic theory for the phase separation of self-propelled repulsive disks, *Europhys. Lett.* **103**, 30008 (2013).
- [6] J. T. Siebert, F. Dittrich, F. Schmid, K. Binder, T. Speck, and P. Virnau, Critical behavior of active Brownian particles, *Phys. Rev. E* **98**, 030601(R) (2018).
- [7] G. S. Redner, M. F. Hagan, and A. Baskaran, Structure and Dynamics of a Phase-Separating Active Colloidal Fluid, *Phys. Rev. Lett.* **110**, 055701 (2013).
- [8] P. Digregorio, D. Levis, A. Suma, L. F. Cugliandolo, G. Gonnella, and I. Pagonabarraga, Full Phase Diagram of Active Brownian Disks: From Melting to Motility-Induced Phase Separation, *Phys. Rev. Lett.* **121**, 098003 (2018).
- [9] P. Nie, J. Chatteraj, A. Piscitelli, P. Doyle, R. Ni, and M. P. Ciamarra, Stability phase diagram of active Brownian particles, *Phys. Rev. Res.* **2**, 023010 (2020).
- [10] J. Palacci, S. Sacanna, A. P. Steinberg, D. J. Pine, and P. M. Chaikin, Living crystals of light-activated colloidal surfers, *Science* **339**, 936 (2013).
- [11] I. Buttinoni, J. Bialké, F. Kümmel, H. Löwen, C. Bechinger, and T. Speck, Dynamical Clustering and Phase Separation in Suspensions of Self-Propelled Colloidal Particles, *Phys. Rev. Lett.* **110**, 238301 (2013).
- [12] G. Liu, A. Patch, F. Bahar, D. Yllanes, R. D. Welch, M. C. Marchetti, S. Thutupalli, and J. W. Shaevitz, Self-Driven Phase Transitions Drive *Myxococcus xanthus* Fruiting Body Formation, *Phys. Rev. Lett.* **122**, 248102 (2019).
- [13] Y. Yang, V. Marceau, and G. Gompper, Swarm behavior of self-propelled rods and swimming flagella, *Phys. Rev. E* **82**, 031904 (2010).
- [14] A. Suma, G. Gonnella, D. Marenduzzo, and E. Orlandini, Motility-induced phase separation in an active dumbbell fluid, *Europhys. Lett.* **108**, 56004 (2014).
- [15] S. E. Moran, I. R. Bruss, P. W. Schönhöfer, and S. C. Glotzer, Particle anisotropy tunes emergent behavior in active colloidal systems, *Soft Matter* **18**, 1044 (2022).
- [16] J. T. Siebert, J. Letz, T. Speck, and P. Virnau, Phase behavior of active Brownian disks, spheres, and dimers, *Soft Matter* **13**, 1020 (2017).
- [17] L. F. Cugliandolo, P. Digregorio, G. Gonnella, and A. Suma, Phase Coexistence in Two-Dimensional Passive and Active Dumbbell Systems, *Phys. Rev. Lett.* **119**, 268002 (2017).
- [18] M. Bär, R. Großmann, S. Heidenreich, and F. Peruani, Self-propelled rods: Insights and perspectives for active matter, *Annu. Rev. Condens. Matter Phys.* **11**, 441 (2020).
- [19] P. W. A. Schönhöfer and S. C. Glotzer, Curvature-controlled geometrical lensing behavior in self-propelled colloidal particle systems, *Soft Matter* **18**, 8561 (2022).
- [20] M. Theers, E. Westphal, K. Qi, R. G. Winkler, and G. Gompper, Clustering of microswimmers: interplay of shape and hydrodynamics, *Soft Matter* **14**, 8590 (2018).
- [21] V. M. Worlitzer, G. Ariel, A. Be'er, H. Stark, M. Bär, and S. Heidenreich, Motility-induced clustering and meso-scale turbulence in active polar fluids, *New J. Phys.* **23**, 033012 (2021).
- [22] R. Matas-Navarro, R. Golestanian, T. B. Liverpool, and S. M. Fielding, Hydrodynamic suppression of phase separation in active suspensions, *Phys. Rev. E* **90**, 032304 (2014).
- [23] A. Zöttl and H. Stark, Hydrodynamics Determines Collective Motion and Phase Behavior of Active Colloids in Quasi-Two-Dimensional Confinement, *Phys. Rev. Lett.* **112**, 118101 (2014).
- [24] H. R. Vutukuri, M. Hoore, C. Abaurrea-Velasco, L. van Buren, A. Dutto, T. Auth, D. A. Fedosov, G. Gompper, and J. Vermant, Active particles induce large shape deformations in giant lipid vesicles, *Nature (London)* **586**, 52 (2020).
- [25] S. C. Takatori and A. Sahu, Active Contact Forces Drive Nonequilibrium Fluctuations in Membrane Vesicles, *Phys. Rev. Lett.* **124**, 158102 (2020).
- [26] J. Stenhammar, D. Marenduzzo, R. J. Allen, and M. E. Cates, Phase behaviour of active Brownian particles: the role of dimensionality, *Soft Matter* **10**, 1489 (2014).
- [27] A. Wysocki, R. G. Winkler, and G. Gompper, Cooperative motion of active Brownian spheres in three-dimensional dense suspensions, *Europhys. Lett.* **105**, 48004 (2014).
- [28] A. Creppy, E. Clément, C. Douarce, M. V. D'Angelo, and H. Auradou, Effect of motility on the transport of bacteria populations through a porous medium, *Phys. Rev. Fluids* **4**, 013102 (2019).
- [29] L. Ritsma, S. I. Ellenbroek, A. Zomer, H. J. Snippert, F. J. De Sauvage, B. D. Simons, H. Clevers, and J. Van Rheenen, Intestinal crypt homeostasis revealed at single-stem-cell level by in vivo live imaging, *Nature (London)* **507**, 362 (2014).
- [30] P. J. Keller, A. D. Schmidt, J. Wittbrodt, and E. H. Stelzer, Reconstruction of zebrafish early embryonic development by scanned light sheet microscopy, *Science* **322**, 1065 (2008).
- [31] L. G. Pimpale, T. C. Middelkoop, A. Mietke, and S. W. Grill, Cell lineage-dependent chiral actomyosin flows drive cellular rearrangements in early caenorhabditis elegans development, *Elife* **9**, e54930 (2020).
- [32] L. Apaza and M. Sandoval, Brownian self-driven particles on the surface of a sphere, *Phys. Rev. E* **96**, 022606 (2017).
- [33] P. Castro-Villarreal and F. J. Sevilla, Active motion on curved surfaces, *Phys. Rev. E* **97**, 052605 (2018).

- [34] Y. Fily, A. Baskaran, and M. F. Hagan, Dynamics and density distribution of strongly confined noninteracting nonaligning self-propelled particles in a nonconvex boundary, *Phys. Rev. E* **91**, 012125 (2015).
- [35] Y. Fily, A. Baskaran, and M. F. Hagan, Active particles on curved surfaces, [arXiv:1601.00324](https://arxiv.org/abs/1601.00324).
- [36] R. Sknepnek and S. Henkes, Active swarms on a sphere, *Phys. Rev. E* **91**, 022306 (2015).
- [37] W. Li, Collective motion of swarming agents evolving on a sphere manifold: A fundamental framework and characterization, *Sci. Rep.* **5**, 13603 (2015).
- [38] C.-P. Hsu, A. Sciortino, Y. A. de la Trobe, and A. R. Bausch, Activity-induced polar patterns of filaments gliding on a sphere, *Nature Commun.* **13**, 2579 (2022).
- [39] L. Janssen, A. Kaiser, and H. Löwen, Aging and rejuvenation of active matter under topological constraints, *Sci. Rep.* **7**, 5667 (2017).
- [40] B.-Q. Ai, B.-Y. Zhou, and X.-M. Zhang, Binary mixtures of active and passive particles on a sphere, *Soft Matter* **16**, 4710 (2020).
- [41] L. Caprini, U. M. B. Marconi, R. Wittmann, and H. Löwen, Dynamics of active particles with space-dependent swim velocity, *Soft Matter* **18**, 1412 (2022).
- [42] M. J. Schnitzer, Theory of continuum random walks and application to chemotaxis, *Phys. Rev. E* **48**, 2553 (1993).
- [43] See Supplemental Material at <http://link.aps.org/supplemental/10.1103/PhysRevResearch.5.033054> for simulation movies.
- [44] S. Das, G. Gompper, and R. G. Winkler, Local stress and pressure in an inhomogeneous system of spherical active Brownian particles, *Sci. Rep.* **9**, 6608 (2019).
- [45] G. Volpe, I. Buttinoni, D. Vogt, H.-J. Kümmerer, and C. Bechinger, Microswimmers in patterned environments, *Soft Matter* **7**, 8810 (2011).
- [46] A. P. Solon, J. Stenhammar, M. E. Cates, Y. Kafri, and J. Tailleur, Generalized thermodynamics of phase equilibria in scalar active matter, *Phys. Rev. E* **97**, 020602(R) (2018).
- [47] R. Wittkowski, A. Tiribocchi, J. Stenhammar, R. J. Allen, D. Marenduzzo, and M. E. Cates, Scalar ϕ^4 field theory for active-particle phase separation, *Nature Commun.* **5**, 4351 (2014).
- [48] R. G. Winkler, A. Wysocki, and G. Gompper, Virial pressure in systems of spherical active Brownian particles, *Soft Matter* **11**, 6680 (2015).
- [49] D. Levis, J. Codina, and I. Pagonabarraga, Active Brownian equation of state: metastability and phase coexistence, *Soft Matter* **13**, 8113 (2017).
- [50] C. F. Lee, Interface stability, interface fluctuations, and the gibbs–thomson relationship in motility-induced phase separations, *Soft Matter* **13**, 376 (2017).
- [51] M. E. Cates and J. Tailleur, Motility-induced phase separation, *Annu. Rev. Condens. Matter Phys.* **6**, 219 (2015).
- [52] I. R. Bruss and S. C. Glotzer, Phase separation of self-propelled ballistic particles, *Phys. Rev. E* **97**, 042609 (2018).
- [53] A. Callegari and G. Volpe, Numerical simulations of active brownian particles, in *Flowing Matter*, edited by F. Toschi and M. Sega (Springer Open, Berlin, 2019), p. 211.
- [54] G. Vizsnyiczai, G. Frangipane, S. Bianchi, F. Saglimbeni, D. Dell’Arciprete, and R. Di Leonardo, A transition to stable one-dimensional swimming enhances e. coli motility through narrow channels, *Nature Commun.* **11**, 2340 (2020).
- [55] M. Paoluzzi, R. Di Leonardo, and L. Angelani, Self-Sustained Density Oscillations of Swimming Bacteria Confined in Microchambers, *Phys. Rev. Lett.* **115**, 188303 (2015).
- [56] K. S. Olsen, L. Angheluta, and E. G. Flekkøy, Escape problem for active particles confined to a disk, *Phys. Rev. Res.* **2**, 043314 (2020).
- [57] M. Souzy, A. Allard, J.-F. Louf, M. Contino, I. Tuval, and M. Polin, Microbial narrow-escape is facilitated by wall interactions, *Phys. Rev. Res.* **4**, L022029 (2022).
- [58] Y.-W. Chang, A. A. Fragkopoulos, S. M. Marquez, H. D. Kim, T. E. Angelini, and A. Fernández-Nieves, Biofilm formation in geometries with different surface curvature and oxygen availability, *New J. Phys.* **17**, 033017 (2015).
- [59] J. Wierchos, A. D. L. Ríos, and C. Ascaso, Microorganisms in desert rocks: the edge of life on earth, *Int. Microbiol.* **15**, 171 (2012).
- [60] R. U. Meckenstock, F. von Netzer, C. Stumpp, T. Lueders, A. M. Himmelberg, N. Hertkorn, P. Schmitt-Kopplin, M. Harir, R. Hosein, S. Haque *et al.*, Water droplets in oil are microhabitats for microbial life, *Science* **345**, 673 (2014).
- [61] M. Delarue, J. Hartung, C. Schreck, P. Gniewek, L. Hu, S. Herminghaus, and O. Hallatschek, Self-driven jamming in growing microbial populations, *Nature Phys.* **12**, 762 (2016).
- [62] L. Hall-Stoodley, J. W. Costerton, and P. Stoodley, Bacterial biofilms: from the natural environment to infectious diseases, *Nature Rev. Microbiol.* **2**, 95 (2004).
- [63] S. C. Takatori and J. F. Brady, Forces, stresses and the (thermo?) dynamics of active matter, *Curr. Opin. Colloid Interface Sci.* **21**, 24 (2016).